Current Biology 19, 95–107, January 27, 2009 ©2009 Elsevier Ltd All rights reserved DOI 10.1016/j.cub.2008.12.029

Article

Molecular Mechanisms of Membrane Deformation by I-BAR Domain Proteins

Juha Saarikangas,[1,5] Hongxia Zhao,[1,5] Anette Pykäläinen,[1] Pasi Laurinmäki,[2] Pieta K. Mattila,[1,6] Paavo K.J. Kinnunen,[3] Sarah J. Butcher,[2] and Pekka Lappalainen[1,4,*]

[1]Program in Cell and Molecular Biology
[2]Program in Structural Biology and Biophysics
Institute of Biotechnology
P.O. Box 56
[3]Helsinki Biophysics & Biomembrane Group
Medical Biochemistry
Institute of Biomedicine
P.O. Box 63
[4]Neuroscience Center
P.O. Box 56
University of Helsinki
FIN-00014 Helsinki
Finland

Summary

Background: Generation of membrane curvature is critical for the formation of plasma membrane protrusions and invaginations and for shaping intracellular organelles. Among the central regulators of membrane dynamics are the BAR superfamily domains, which deform membranes into tubular structures. In contrast to the relatively well characterized BAR and F-BAR domains that promote the formation of plasma membrane invaginations, I-BAR domains induce plasma membrane protrusions through a poorly understood mechanism.

Results: We show that I-BAR domains induce strong PI(4,5)P_2 clustering upon membrane binding, bend the membrane through electrostatic interactions, and remain dynamically associated with the inner leaflet of membrane tubules. Thus, I-BAR domains induce the formation of dynamic membrane protrusions to the opposite direction than do BAR and F-BAR domains. Strikingly, comparison of different I-BAR domains revealed that they deform PI(4,5)P_2-rich membranes through distinct mechanisms. IRSp53 and IRTKS I-BARs bind membranes mainly through electrostatic interactions, whereas MIM and ABBA I-BARs additionally insert an amphipathic helix into the membrane bilayer, resulting in larger tubule diameter in vitro and more efficient filopodia formation in vivo. Furthermore, FRAP analysis revealed that whereas the mammalian I-BAR domains display dynamic association with filopodia, the *C. elegans* I-BAR domain forms relatively stable structures inside the plasma membrane protrusions.

Conclusions: These data define I-BAR domain as a functional member of the BAR domain superfamily and unravel the mechanisms by which I-BAR domains deform membranes to induce filopodia in cells. Furthermore, our work reveals unexpected divergence in the mechanisms by which evolutionarily distinct groups of I-BAR domains interact with PI(4,5)P_2-rich membranes.

Introduction

In addition to the well-established role of the cytoskeleton in producing forces to generate plasma membrane protrusions and invaginations, many membrane-associated proteins have also been shown to directly sculpt biological membranes. These proteins generate membrane curvature through insertion of hydrophobic or amphiphatic motifs into the membrane to induce bilayer asymmetry and through the formation of membrane-bound protein scaffolds with intrinsic curvature [1–8].

The BAR (Bin, Amphiphysin, Rvs) domain superfamily of proteins are central regulators of membrane remodeling in all eukaryotes. Mutations in genes encoding BAR domain proteins have been linked to many diseases [9–11], and inactivation of these proteins in cells and animals is often characterized by severe phenotypes resulting from altered membrane dynamics [12–14]. Based on structural features and phylogenetic relationships, the BAR domains can be divided into distinct subfamilies [15].

The canonical BAR domain is a dimeric module, where three kinked antiparallel α helices of each monomer form a banana-shaped dimeric 6-helix bundle [16]. BAR domains interact with cellular membranes through their concave surface, which typically contains charged amino acids [16]. A subset of BAR domains (N-BARs) also contain an N-terminal amphiphatic helix that folds upon membrane interaction and penetrates into the bilayer [16–18]. In a number of proteins, the BAR domain is also functionally linked to other membrane-binding motifs such as PH or PX domains [19–21]. Thus, although the curved shape of BAR domains appears to be critical for membrane tubulation, in many cases the membrane curvature-sensing/generation activity is enhanced by additional lipid-binding motifs.

F-BAR domain was originally identified as a FER-CIP4 homology (FCH) domain in the N-terminal region of many actin-regulating proteins. Subsequent studies revealed overall sequence homology between FCH and BAR domains and demonstrated that F-BAR (FCH and BAR) domains tubulate membranes in vitro and in vivo like BAR domains [13, 22]. The structure of F-BAR domain differs from the canonical BAR domain by containing five α helices per monomer. Importantly, being more elongated and gently curved, F-BAR domains induce thicker membrane tubules in comparison to BAR domains [23–25]. A recent cryo-EM study demonstrated that F-BAR domains self-assemble into a helical coat around the membrane tubules, providing evidence that these domains use a combination of scaffolding and cooperative assembly to induce membrane curvature [26].

The I-BAR domain, which is also known as IM (IRSp53/MIM homology) domain, was first identified as an F-actin crosslinking domain at the N-terminal region of mammalian IRSp53 and missing-in-metastasis (MIM) proteins [27]. However, subsequent studies suggested that I-BAR/IM domains do not significantly crosslink actin filaments under physiological

*Correspondence: pekka.lappalainen@helsinki.fi
[5]These authors contributed equally to this work
[6]Present address: Cancer Research UK London Research Institute, 44 Lincoln's Inn Fields, London WC2A 3PX, UK

conditions and revealed that the domain displays structural homology to BAR domains [28–30]. I-BAR/IM monomer consists of three α helices that dimerize into an antiparallel structure, which resembles a zeppelin or inverse BAR (I-BAR) domain shape. Biochemical studies demonstrated that I-BAR domains of MIM and IRSp53 directly bind and deform membranes into tubules in vitro [30, 31]. However, in contrast to the concave-shaped lipid-binding interface of BAR and F-BAR domains, the positively charged lipid-binding surface of I-BAR domains displays a convex geometry [30, 31]. This provided a possible structural explanation for why I-BAR domains induce membrane protrusions rather than invaginations when expressed in cells [27, 32, 33]. However, direct evidence for this "inverse mechanism" has not been demonstrated. Furthermore, possible differences in the membrane deformation properties within the I-BAR domain family (there are five I-BAR domains proteins in mammals, two in *Drosophila*, and one in *C. elegans*) have not been examined [34].

Here, we demonstrate that I-BAR domains bind to the inner leaflet of membrane tubules, thereby inducing the formation of dynamic membrane tubules in the opposite orientation to that of BAR and F-BAR domains. Furthermore, by comparing the membrane interactions of different vertebrate I-BAR domains and their *C. elegans* homolog, we reveal that different I-BAR domains utilize partially distinct mechanisms to deform membranes. These results provide important new mechanistic insights into the role of I-BAR proteins in the formation of plasma membrane protrusions such as filopodia.

Results

I-BAR Domains Bind to the Inner Leaflet of Membrane Tubules and Thereby Deform Membranes in the Opposite Direction to that of BAR Domains

To examine the directionality and dynamics of I-BAR domain-induced membrane tubules in vitro, we monitored their effects on giant unilamellar vesicles (GUVs). Because GUVs are relatively large ($\sim$5–500 μm) and thus have similar tension properties to that of cellular membranes, they are considered good models to monitor protein-induced membrane deformation in vitro [35]. Within 20–200 s after addition of MIM I-BAR, dynamic membrane tubules that invaginated toward the interior of GUVs appeared. At longer incubation times, these multiple invaginations led to the shrinkage of the GUVs (Figure 1A and data not shown). In contrast, the N-BAR domain induced long outward protrusions at the surface of the GUV that in many cases resulted in the breakdown of the vesicle within $\sim$100–200 s after addition of the protein (Figure 1B).

To reveal whether I-BAR domains indeed bind to the inner leaflet of the membrane tubules, as expected from the orientation of the I-BAR domain-induced membrane tubules on GUVs, we incubated I-BAR domains with multilamellar vesicles (MLVs) that were subsequently visualized by cryo transmission electron microscopy (cryo-EM). The morphology of the membrane structures in the electron micrographs fell under two distinct classes: tubular structures and spherical vesicles (Figures 1C–1F). Comparison of different I-BAR domains revealed that the tubules induced by the mammalian MIM and IRSp53 I-BARs were less uniform than the ones induced by the *C. elegans* I-BAR. MIM and IRSp53 I-BAR-induced membrane tubules typically contained perpendicularly oriented striations at the inner leaflet, indicating that these domains indeed associate with the inner leaflet of the membrane tubules (Figures 1C and 1D). Similar striations were not observed in MLVs incubated with the *C. elegans* I-BAR domain, although the inner leaflet of the membrane tubules induced by the *C. elegans* I-BAR appeared thicker and more electron dense in the images. To detect the location of the *C. elegans* I-BAR domain in the membrane tubules, electron-density profiles of the membrane with and without I-BAR domains were compared. For this purpose, perpendicular density profiles of 20 randomly picked tubule sections and spherical vesicles were calculated. Density profiles demonstrated that in the *C. elegans* I-BAR-induced membrane tubules, additional electron density (Figure 1E inset, area shaded by red lines) was always detected at the inner face of the inner membrane leaflet, whereas no additional density was detected at the inner leaflet of vesicles exhibiting spherical morphology (Figures 1E and 1F). Together, these data demonstrate that I-BAR domains deform membranes by binding to the inner leaflet of the membrane tubules.

I-BAR Domains Cluster PI(4,5)P_2 upon Membrane Binding

Previous studies established that I-BAR domains interact with phospholipid-rich membranes through positively charged patches located at the distal ends of the I-BAR domain [30, 31, 36]. The possible effects of I-BAR domains on PI(4,5)P_2 were first examined by microscopy of GUVs containing NBD-labeled phosphatidylcholine (PC) and bodipy-TMR-labeled PI(4,5)P_2. As a control, we used BSA, which had no visible effects on the morphology of the GUVs or their lipid distribution. Interestingly, in addition to the membrane invaginations and protrusions described in the previous paragraph above, I-BAR and amphiphysin N-BAR domains induced visible clustering of PI(4,5)P_2 on GUVs. The PI(4,5)P_2 clusters were stable and rarely dissociated once formed. Importantly, fluorescently labeled PC did not typically cocluster with PI(4,5)P_2, demonstrating that the bright PI(4,5)P_2 spots on GUVs are not a result of general membrane clustering/ruffling at certain foci (Figure 2A). Importantly, PI(4,5)P_2 clustering was typically associated with the formation of membrane tubules (Figure 2B).

To quantify PI(4,5)P_2-clustering activities of different I-BARs, the self quenching of Bodipy-TMR-PI(4,5)P_2 resulting from clustering upon addition of protein was monitored by measuring fluorescence intensity. All the I-BAR domains tested and the amphiphysin N-BAR domain resulted in self quenching of the fluorescent probe molecules (Figure 2B). The results were plotted (equations are given in the Supplemental Experimental Procedures available online) to obtain values for PI(4,5)P_2 clustering of each protein at different concentrations. These data suggest that the IRSp53 I-BAR domain induced the strongest clustering of PI(4,5)P_2, whereas the MIM and ABBA I-BARs were $\sim$15% less efficient in clustering PI(4,5)P_2. Also, the amphiphysin N-BAR domain clustered PI(4,5)P_2, but significantly less efficiently than I-BARs. Furthermore, these experiments revealed that the positively charged "lipid-binding interface" of the I-BAR domains is essential for PI(4,5)P_2 clustering, because neutralization of positively charged residues at these regions correlated with a decrease in the capacity of the I-BAR domain to cluster PI(4,5)P_2 (Figure 2C; Figure S1). We also tested whether I-BAR domains are capable of clustering another negatively charged lipid, phosphatidylserine (PS). Importantly, the I-BAR domains induced only very weak clustering of PS, whereas the amphiphysin BAR domain clustered PS nearly as efficiently as PI(4,5)P_2 (Figure 2E).

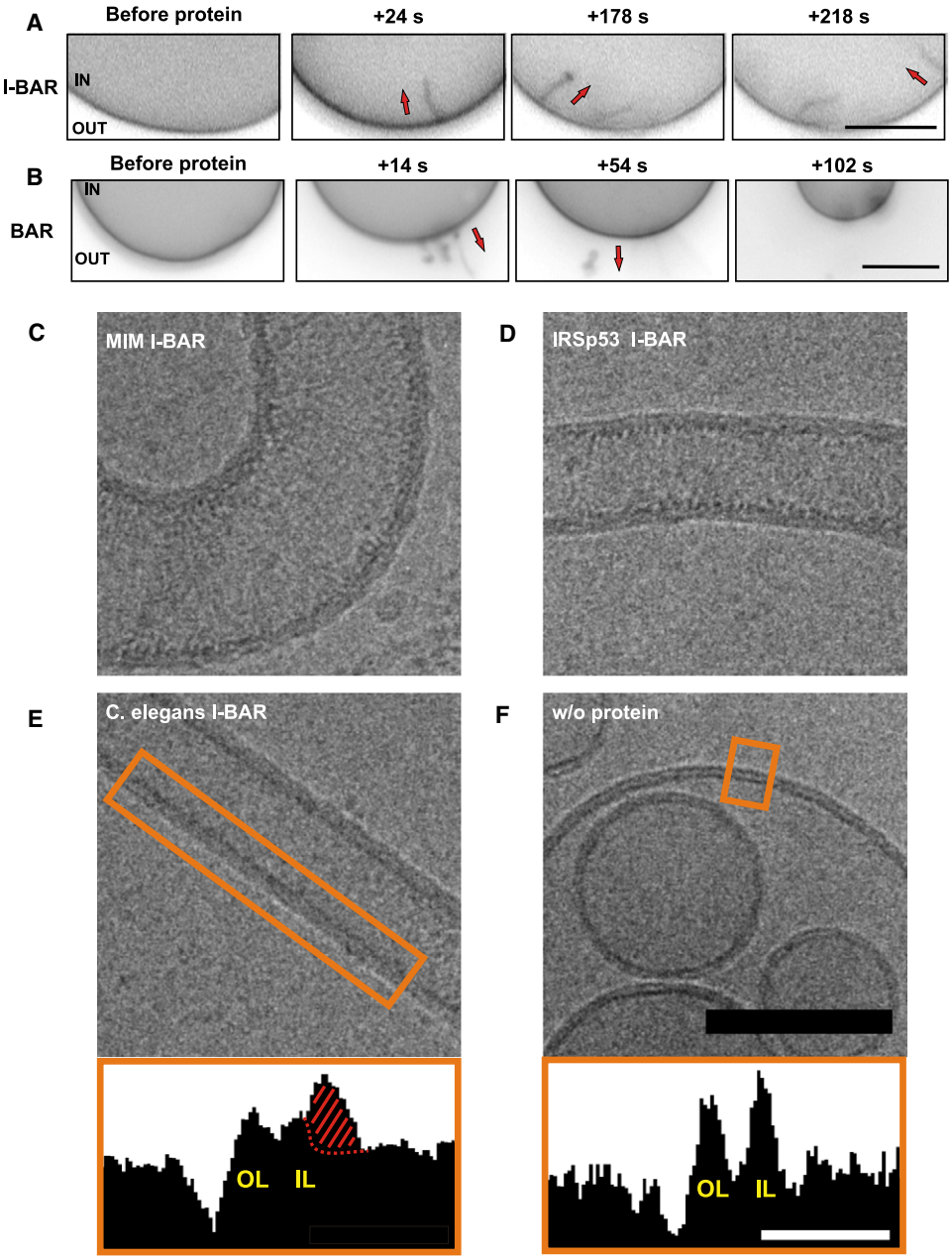

Figure 1. I-BAR Domains Induce Negative Membrane Curvature by Binding to the Interior of the Membrane Tubules

(A and B) Time-course analysis of giant unilamellar vesicles (GUVs) incubated with MIM I-BAR domain (A) or amphiphysin N-BAR domain (B). Both proteins induced tubulation of vesicles, but to opposite directions. N-BAR domain-induced membrane tubules point outwards from the vesicle, whereas I-BARs induced tubules invaginate toward the interior of the vesicle. Scale bars represent 10 μm.

(C–F) Representative cryo-EM micrographs showing morphology of the membrane tubes induced by MIM, IRSp53, *C. elegans* I-BAR domain, and the control vesicles. In MIM and IRSp53 I-BAR domain-induced tubules, clear striations were visible on the inner leaflet of the membrane tubules, indicating bound protein. Scale bar represents 100 nm. Insets in (E) and (F): The orange rectangle denotes the areas from which the density profiles were calculated and plotted in the graph shown on the bottom of the image. The graphs demonstrate that in the spherical control vesicle, the inner leaflet (IL) and the outer leaflet (OL) have similar density profiles, whereas in the *C. elegans* I-BAR-induced membrane tubule, the inner leaflet has additional electron density (shaded with red lines) as compared to the outer leaflet. Graph scale bar represents 10 nm.

Different I-BAR Domains Induce the Formation of Membrane Tubules with Distinct Diameters Both In Vitro and In Vivo

A phylogenetic analysis shows that mammalian I-BAR domains can be divided into two evolutionarily diverged subfamilies: one consisting of MIM and ABBA, and the other one consisting of IRSp53, IRTKS, and FLJ22582 (Figure 3A). To examine possible differences in membrane interactions between I-BAR domains, we visualized multilamellar vesicles incubated with MIM, ABBA, IRSp53, IRTKS, and *C. elegans* I-BAR domains with transmission electron microscopy (TEM). The mouse FLJ22582 I-BAR domain construct (residues 1–239) displayed poor solubility when expressed in *E. coli* and therefore was not included in the analysis. All tested I-BARs

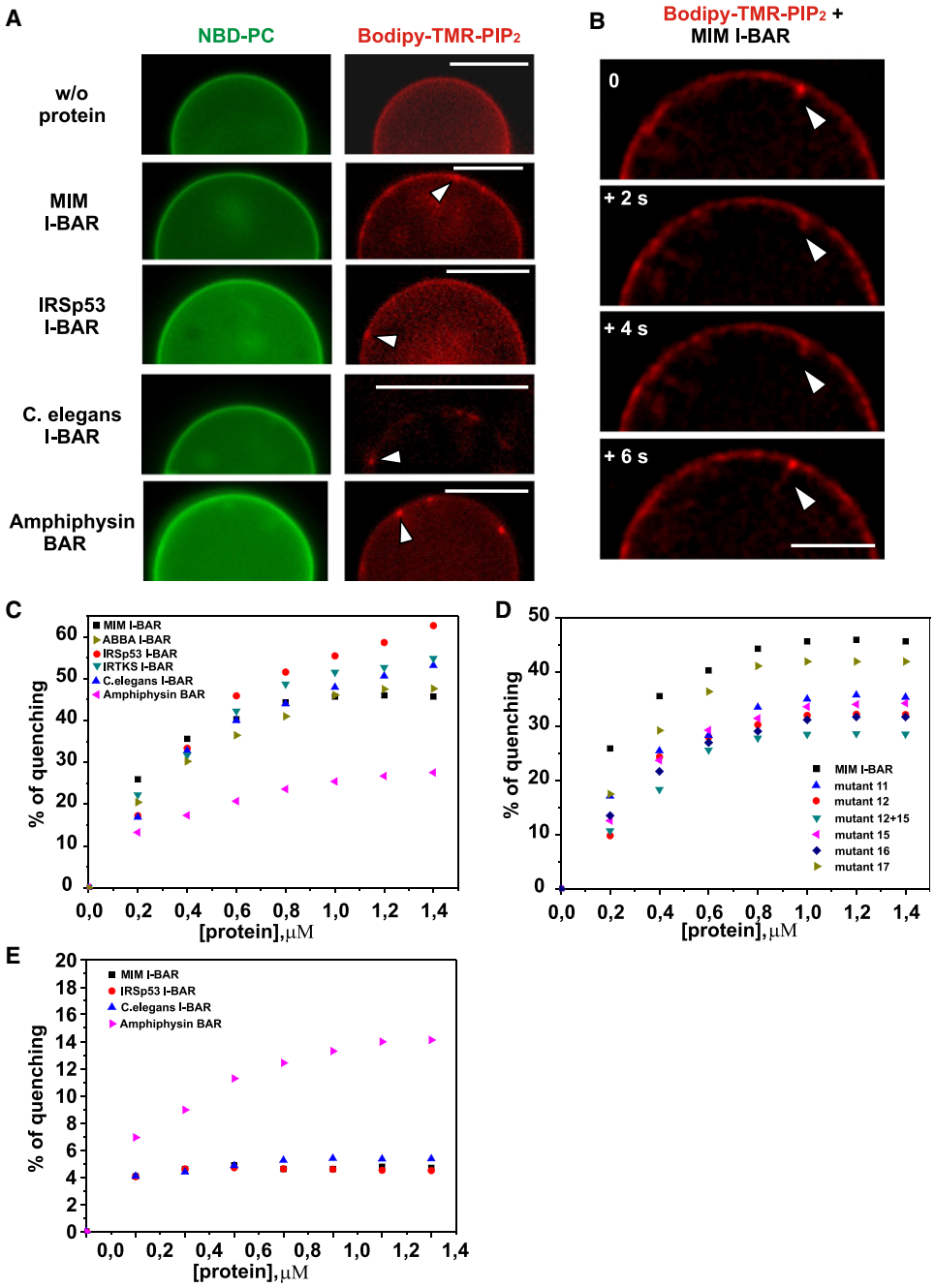

Figure 2. I-BAR Domains Induce Clustering of PI(4,5)P_2

(A) Images from GUVs incubated with different BAR domains or control protein (BSA). All BAR domains tested induced clustering of PI(4,5)P_2 (red), whereas no clustering was seen in phosphatidylcholine (PC) (green) channel.

(B) Time-lapse images of a GUV show the clustering of PI(4,5)P_2 (red) preceding the formation of a membrane tubule (arrowhead). Scale bars represent 10 μm.

(C) The clustering of PI(4,5)P_2 was further assayed by monitoring the self-quenching of Bodipy-TMR-PI(4,5)P_2 in the presence and absence of BAR domains.

(D) Mutations in the positively charged residues at the lipid-binding interface of MIM I-BAR domain resulted in impaired clustering of PI(4,5)P_2.

(E) I-BARs cluster PS only very weakly, whereas amphiphysin BAR domain clusters PS almost as efficiently as does PI(4,5)P_2.

deformed membranes into tube-like structures (Figure 3B). Surprisingly, despite the structural similarity within the I-BAR domains [28, 29], significant differences in the diameters of the membrane tubules induced by different I-BAR domains were detected. The tubules induced by MIM (60 nm) and ABBA (55 nm) were significantly thicker than the ones induced by IRSp53 (43 nm), IRTKS (40 nm), and *C. elegans* (41 nm) I-BAR domains ($p < 0.001$, one-way ANOVA) (Figure 3C). Similar results were also obtained when the assay was carried out with unilamellar vesicles (Figure S2B).

When coexpressed in U2OS cells, I-BAR domains (fused to either GFP or Cherry fluorescent tags) that induce the formation of tubules of distinct diameters in vitro segregated into different compartments at the membranes (Figure 3D). The

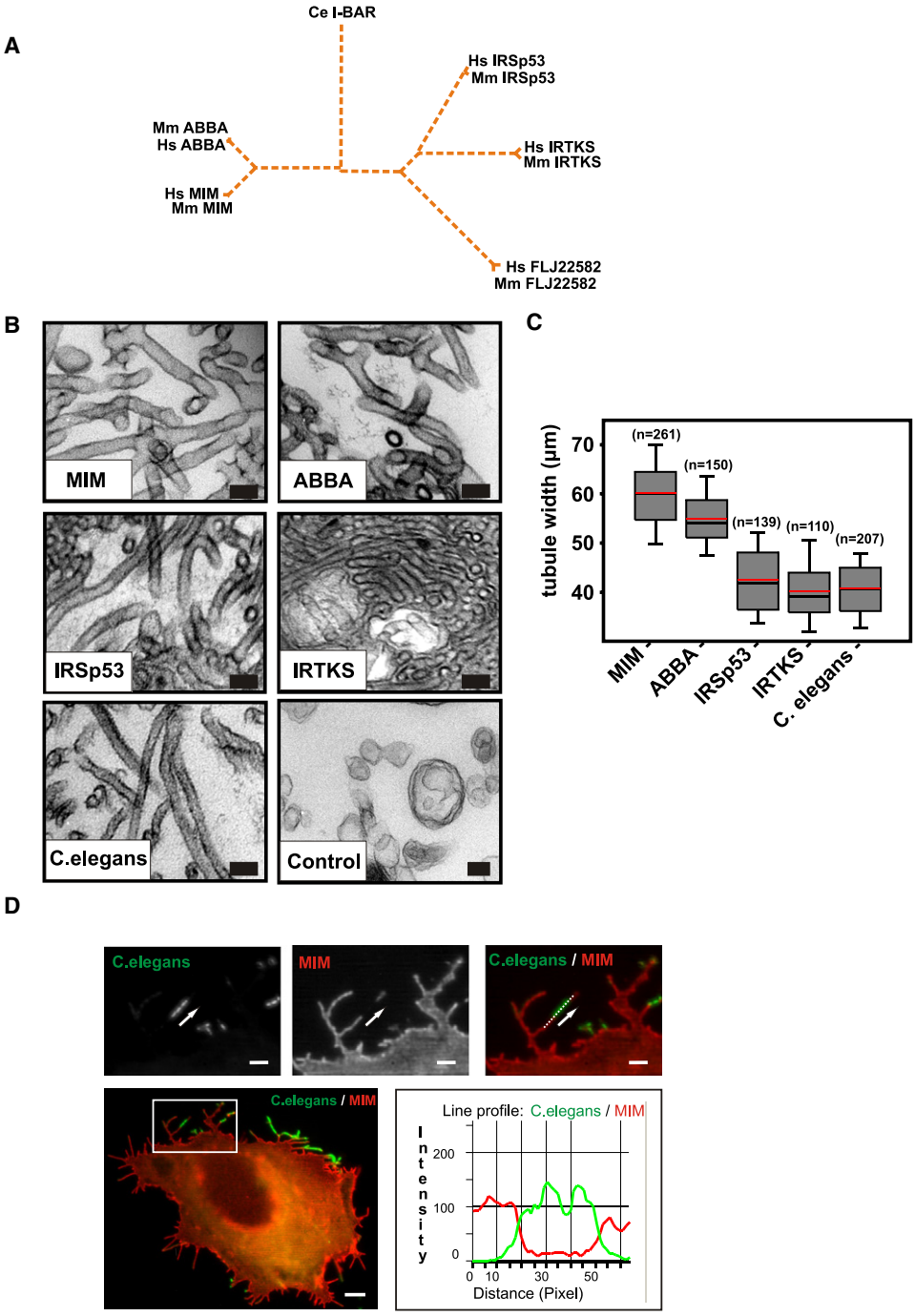

Figure 3. I-BARs Domains Induce the Formation of Tubules with Distinct Diameters In Vitro and In Vivo

(A) A phylogenetic tree based on an amino acid sequence alignment of human (Hs), mouse (Mm), and *C. elegans* (Ce) I-BAR domains demonstrates that these domains can be divided into different branches.

(B) TEM micrographs from vesicles incubated with different I-BARs. Scale bar represents 0.1 μm.

(C) Quantification of tube widths from electron micrographs shows that MIM and ABBA I-BARs induce thicker tubes than do IRSp53, IRTKS, and *C. elegans* I-BARs. Red and black lines in the plot indicate mean and median, respectively. The top box represents 75th and bottom box 25th percentiles and the bars 90th and 10th percentiles, respectively.

(D) Image of an U2OS cell simultaneously transfected with *C. elegans* I-BAR-GFP (green) and MIM I-BAR-Cherry (red). The line intensity profile measured along the line indicated in the inset demonstrates that these proteins segregate into distinct compartments in filopodia. Scale bars represent 5 μm and 2 μm for the insets.

differences in distribution of the protein pairs was further validated by measuring the intensity of both channels on a line drawn along the I-BAR domain-induced filopodia. As a control, the cells were transfected with both Cherry and GFP-tagged MIM I-BAR expression constructs, which showed very similar fluorescence intensities along the line in both channels.

Furthermore, when coexpressed in cells, MIM and ABBA as well as IRTKS and IRSp53 I-BARs, which in vitro induce the formation of membrane tubules of similar diameters, did not segregate into distinct compartments in filopodia (Figures S3A, S3B, and S3D). However, clear segregation into distinct filopodia or filopodial compartments was detected when MIM I-BAR domain was coexpressed with either IRSp53 or *C. elegans* I-BAR domain (Figure 3D; Figure S3C and Movie S1). Surprisingly, despite the similar tubule diameter in vitro, IRSp53 and *C. elegans* I-BAR domains also segregated into different compartments when expressed in cells (Figure S3E). This may result from the very stable association of *C. elegans* I-BAR domain in filopodia as compared to mammalian I-BAR domains (see Discussion).

I-BAR Domains of MIM and ABBA Insert Their N-Terminal Amphiphatic Helix into the Membrane Bilayer

To test whether MIM and IRSp53 I-BAR domains interact with membranes differently when electrostatic interactions are compromised, a cosedimentation assay with I-BARs and membranes was carried out at different salt concentrations. At physiological salt, both domains efficiently cosedimented with membranes. At 400 mM NaCl, the interaction between the IRSp53 I-BAR domain and membranes was severely diminished. The MIM I-BAR domain, however, still efficiently cosedimented with membranes, suggesting that besides electrostatic interactions, MIM I-BAR may harbor additional mechanisms to bind membranes (Figure 4A).

To examine whether I-BARs are capable in inserting part(s) of the domain into the membrane bilayer, we studied steady-state fluorescence anisotropy of a membrane probe 1,6-diphenyl 1,3,5-hexatriene (DPH). DPH locates into the hydrophobic core of a lipid bilayer without affecting the physical properties of the membranes and can thus be used for monitoring changes in the trans-gauche isomerization of phospholipid acyl chains in the membrane interior [37]. Binding of MIM and ABBA I-BAR domains to PI(4,5)P_2-containing membranes induced a significant increase in DPH anisotropy, suggesting that these domains insert into the acyl chain region of the bilayer. Also, *C. elegans* I-BAR domain inserted into the lipid bilayer, but changes in the DPH anisotropy were weaker compared to that of MIM and ABBA I-BARs. Importantly, IRSP53 and IRTKS I-BAR domains had no significant effect on DPH anisotropy, indicating that these two "salt-sensitive" I-BARs do not insert into the acyl chain region of the bilayer (Figure 4B).

To test whether the N-terminal amphipatic α helix present in I-BARs of MIM and ABBA (see Figure S3A) is responsible for the membrane insertion, we deleted the first 11 amino acids from the N terminus of MIM I-BAR domain (MIMΔN). When compared to the wild-type I-BAR domain of MIM, the deletion had no effect on the binding affinity to the membranes as measured by cosedimentation assay (data not shown). However, the effect of MIMΔN I-BAR on DPH anisotropy was dramatically decreased compared to the wild-type MIM I-BAR, demonstrating that the N-terminal α helix is critical for membrane insertion. In contrast, the mutants with reduced affinity to PI(4,5)P_2 inserted into the membrane bilayer similarly to the wild-type MIM I-BAR, indicating that strong electrostatic interactions are not critical to the membrane insertion of MIM I-BAR (Figure 4C). Accordingly, MIM-I-BAR induced an increase in the DPH anisotropy also in the absence of PI(4,5)P_2 and at high salt conditions (400 mM) (data not shown). However, when using zwitterionic membrane (PC/PE = 8/2) to completely abolish all negative charges from the membrane, insertion of MIM I-BAR was clearly reduced (Figure S4B), suggesting that membrane insertion still required weak electrostatic interactions.

Based on EM analysis of multilamellar vesicles, the membrane tubulation activity of MIM I-BAR gradually decreased when the salt concentration was increased, indicating the importance of electrostatic interactions in the formation of membrane tubules by I-BAR domains (Figure S2A). Furthermore, we did not detect "inverse" tubulation by MIM I-BAR at high salt, suggesting that despite its membrane-inserting amphipathic N-terminal helix, the MIM I-BAR domain is not capable in bending membranes in the same direction as N-BARs when the electrostatic interactions are eliminated.

To estimate the depth of the membrane insertion, we generated mutant MIM I-BARs, which contain only one tryptophan (Trp) residue located at either position 4 or position 30 of the N-terminal α helix. To examine whether Trp4 and Trp30 insert into the membrane, we first used acrylamide, a neutral, water-soluble quencher of Trp fluorescence. The quenching of Trp by acrylamide was recorded in the absence and presence of lipid vesicles and data analyzed by Stern-Volmer plots. The fluorescence intensity of both Trp4 and Trp30 decreased in a concentration-dependent manner after the addition of acrylamide both in the absence and presence of liposomes without other effects on the spectra (data not shown). However, the decrease in fluorescence intensity was weaker in the presence of liposomes, demonstrating that Trp4 and Trp30 are less accessible to the quencher and thus most likely buried in the bilayer. As compared to Trp30, Trp4 is located in a more hydrophobic environment in the absence of liposomes, but in the presence of liposomes became more accessible to the aqueous quencher as compared to Trp30 (Figure 4D). This suggests that Trp4 is less buried in the bilayer. To measure the depth of Trp4 and Trp30 in the bilayer, we used bromine-labeled lipids, collisional quenchers that are present in the hydrocarbon phase of the bilayer. These lipids are brominated at different positions along the lipid acyl chains and can be used for estimating the depth of Trp insertion in the bilayer. Trp30 was quenched by 9, 10-Br_2-PC and 11, 12-Br_2-PC, whereas no quenching was observed by 6, 7-Br_2-PC. Calculations via the parallax method suggest that Trp30 locates at a depth of 7.3 Å from the center of the bilayer. In contrast, no significant quenching of Trp4 was observed by the two deep quenchers, 9, 10-Br_2-PC and 11, 12-Br_2-PC, but the shallower quencher 6, 7-Br_2-PC quenched Trp4 (Figures 4E and 4F). This suggests that Trp4 locates at a depth of approximately 10.8 Å from the center of the bilayer. Control experiments carried out with IRSp53 I-BAR mutants containing a tryptophan residue at position 3 or 31 provided further evidence that the N-terminal helix of IRSp53 I-BAR does not insert into the membrane bilayer (Figures S4C–S4E).

Insertion of the N-Terminal Helix Affects the Membrane Tubule Diameter In Vitro and Filopodia Formation In Vivo

To elucidate the role of the N-terminal amphipathic helix of MIM I-BAR in membrane tubulation, we mixed vesicles with MIM I-BAR or MIMΔN I-BAR and visualized them with TEM (Figure 5A). Interestingly, although MIMΔN efficiently induced the formation of membrane tubules, the diameter of MIMΔN tubules (45.9 nm) was significantly smaller than that of wild-type MIM I-BAR tubules (60.2 nm; $p < 0.001$, Student's t test) (Figure 5B). Importantly, deletion of 11 N-terminal residues

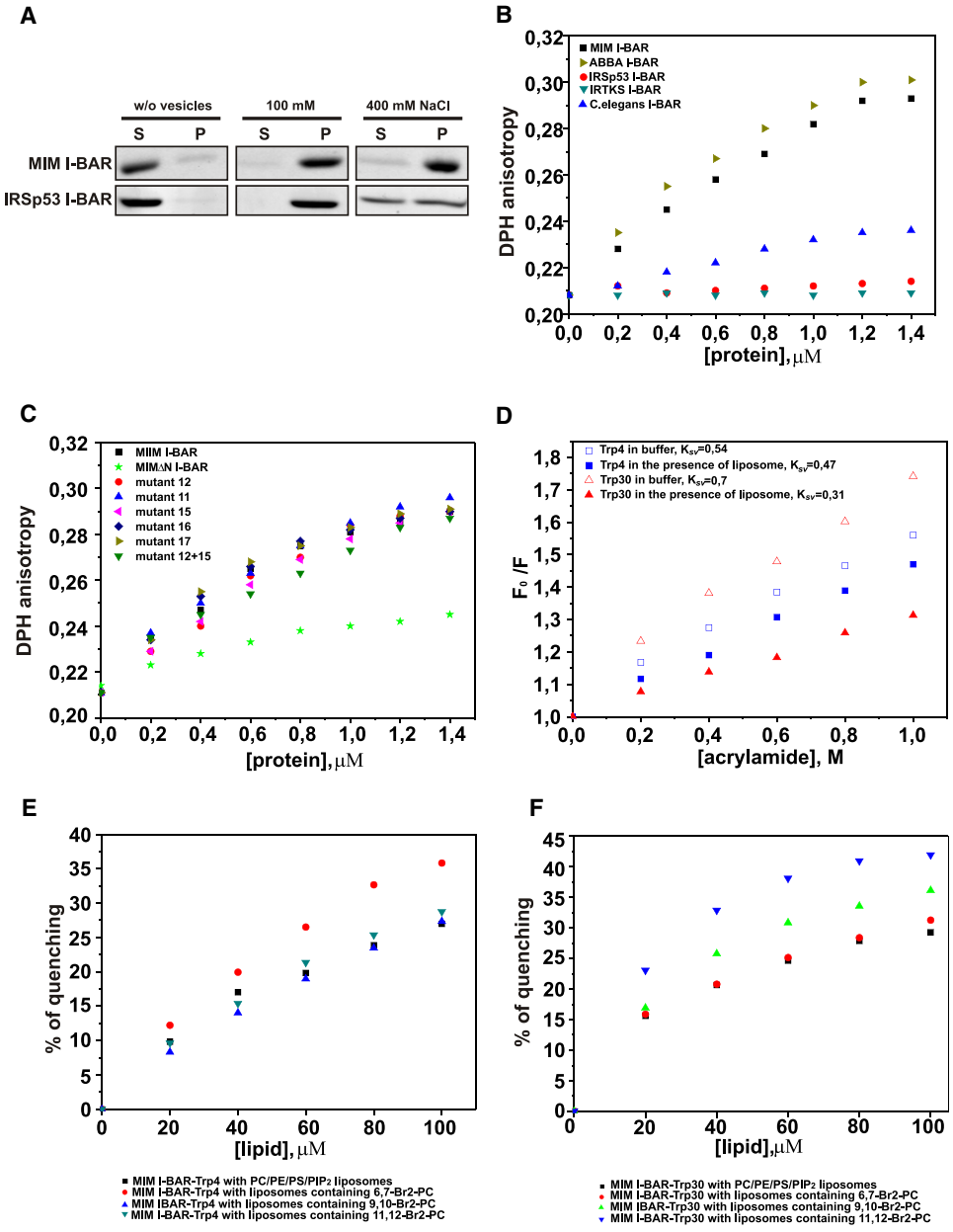

Figure 4. MIM and ABBA I-BAR Domains Insert an Amphipathic α Helix into the Membrane Bilayer

(A) Salt-sensitivity assay demonstrates that IRSp53 I-BAR domain binding to the membrane is more sensitive to salt than is the MIM I-BAR domain. I-BAR domains were incubated with or without vesicles in 100 mM or 400 mM NaCl followed by ultracentrifugation and SDS-PAGE analysis. S, supernatant fraction; P, pellet fraction.

(B) MIM, ABBA, and *C. elegans* I-BAR domains induce an increase in steady-state DPH anisotropy, indicating that these proteins insert into the bilayer. IRSp53 and IRTKS had no detectable effects on DPH anisotropy.

(C) MIM I-BAR domain mutants where positively charged residues were neutralized showed similar insertion profile as wild-type I-BAR, whereas deletion of 11 N-terminal amino acids from MIM I-BAR (MIMΔN) resulted in a significant decrease in DPH anisotropy.

(D) The tryptophans introduced at positions 4 and 30 of the N-terminal α helix of MIM I-BAR are buried in the bilayer as demonstrated by Stern-Volmer plots for the quenching of MIM-I-BAR by acrylamide in an aqueous buffer (open symbol) and in the presence of liposomes (filled symbols).

(E and F) Quenching of tryptophans with brominated lipids indicates that Trp30 and Trp4 are located at depths of approximately 7.3 Å and 10.8 Å from the center of the bilayer, respectively.

from the IRSp53 I-BAR domain did not have significant effect on the tubule width as compared to the wild-type domain (data not shown). Measuring the width of the I-BAR domain-induced filopodia in cells proved difficult, because these tubular protrusions also contain bundles of actin, which made them more variable in diameter (data not shown). However, by measuring the number of filopodia induced by different I-BAR constructs, we found a significant difference between the number of filopodia induced by the I-BARs. The I-BAR domains that insert their N-terminal α helix into the bilayer (wild-type MIM and ABBA I-BARs) were more efficient in inducing filopodia compared to the ones that do not insert

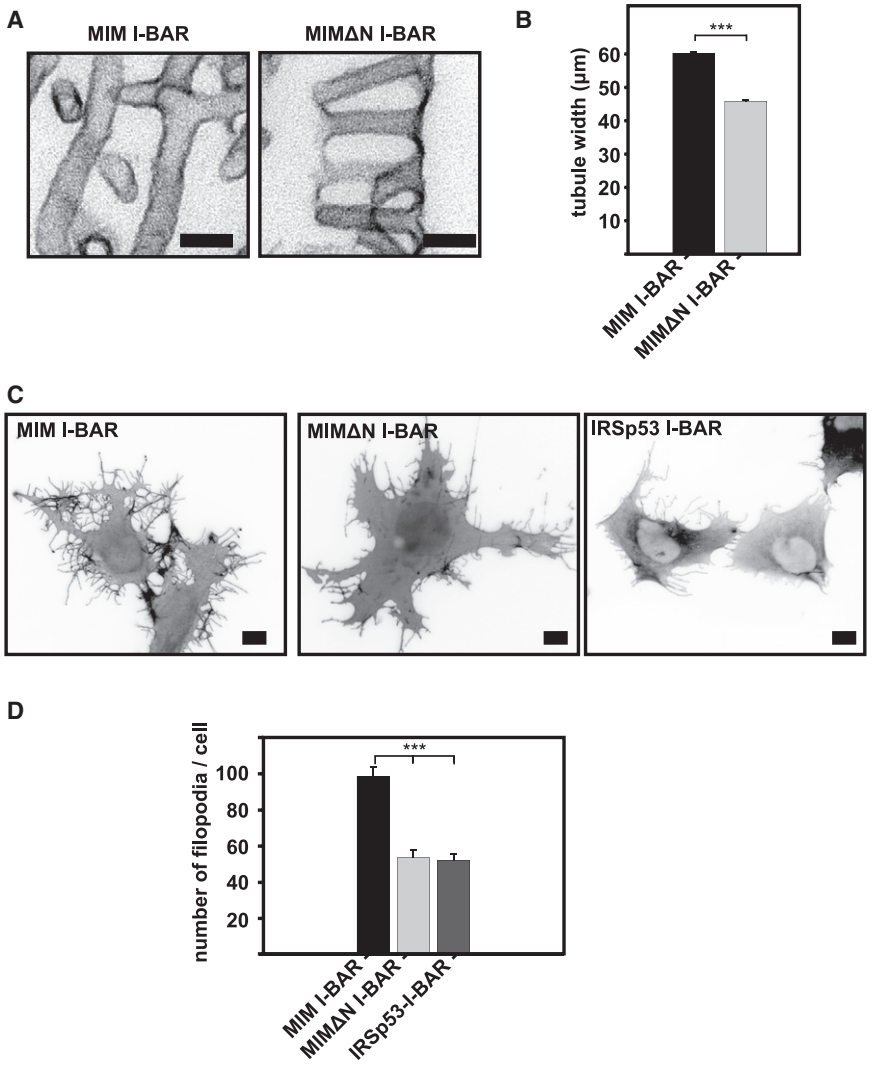

Figure 5. Membrane Insertion of the N-Terminal Helix of MIM I-BAR Regulates the Diameter of Membrane Tubules In Vitro and Their Formation In Vivo

(A) TEM micrographs of typical membrane tubules induced by MIM or MIMΔN I-BARs.

(B) Quantification of diameters of tubules demonstrates that the MIMΔN forms significantly thinner structures than the ones induced by wild-type MIM I-BAR ($p < 0.001$; Student's t test).

(C) MIM I-BAR induces filopodia more efficiently than do MIMΔN or IRSp53 I-BAR. Scale bars represent 10 μm.

(D) Quantification of the average number of filopodia per cell. Error bars represent SEM values. $p < 0.001$ (one-way ANOVA), $n > 30$.

(IRSp53, IRTKS, and MIMΔN) (Figures 5C and 5D; data not shown) ($p < 0.001$, one-way ANOVA).

The Dynamics of I-BAR Domains in Filopodia Measured by FRAP

Upon interaction with membranes, F-BAR domains assemble into helical coats that are held together by lateral and tip-to-tip interactions [26]. To elucidate possible intermolecular interactions of I-BAR domains, we measured their exchange rate in filopodia by using fluorescence recovery after photobleaching (FRAP). U2OS cells were transfected with GFP-tagged I-BARs, GFP fluorescence was photobleached at a region of filopodia, and the rate of fluorescence recovery was measured. The recovery of MIM and IRSp53 I-BARs was rapid with $t_{1/2}$ of 8.3 s and 5.2 s, respectively. Interestingly, in the majority of the filopodia, the recovery of *C. elegans* I-BAR was >10-fold slower with an average $t_{1/2}$ of 85.9 s (Figures 6A and 6B). However, in some wider and more irregular filopodia induced by the *C. elegans* I-BAR domain, the fluorescence recovery was much faster compared to that of thin, regular filopodia present in the same cell (Figure 6C). This suggests that the *C. elegans* I-BAR domain, when oligomerized in the right conformation, can form relatively stable contacts with its neighbors. This is supported by our findings from cryo-EM experiments, in which the *C. elegans* I-BAR appeared to form membrane tubules with a more regular diameter (Figures 1C–1E). Furthermore, live-cell imaging experiments demonstrated that the filopodia induced by the *C. elegans* I-BAR domain are more rigid than the filopodia induced by vertebrate I-BARs (Movie S1). Because MIM I-BAR recovered almost as fast as MIMΔN and IRSp53 I-BARs, the insertion of the N-terminal α helix is most likely not responsible for the slow recovery observed in the case of *C. elegans* I-BAR (Figures 6A and 6B; data not shown).

I-BAR Domain-Induced Membrane Protrusions Display Filopodial Characteristics

I-BAR domains, when expressed in cells, induce actin containing filopodia-like protrusions. However, whether these structures are just morphologically filopodia-like membrane protrusions or if they indeed also harbor other characteristics typical of filopodia has not been reported. Thus, we examined the localization of filopodial markers [38] to I-BAR domain-induced membrane protrusions. U2OS, HeLa, and COS-7 cells were transfected with GFP-tagged MIM and IRSp53 I-BARs as well as constructs encoding full-length proteins, and stained with myosin-10 antibody [39]. Importantly, endogenous myosin-10 often localized to the tips or shafts of membrane protrusions in cells transfected with the full-length proteins or the I-BAR (Figure S5A). U2OS cells were also cotransfected with MIM I-BAR and myosin-10-GFP or with the other well-characterized filopodial markers, fascin-GFP and VASP-GFP. Similar to endogenous filopodia, fascin localized to the shaft of I-BAR-induced protrusions, VASP was found both in the shaft and tip of these protrusions, and myosin-10 was predominately localized at the tips, occasionally being found moving along the filopodial shaft (Figure S5B and Movie S2).

Discussion

The findings presented here define the I-BAR domain as a functional member of the BAR domain superfamily and reveal

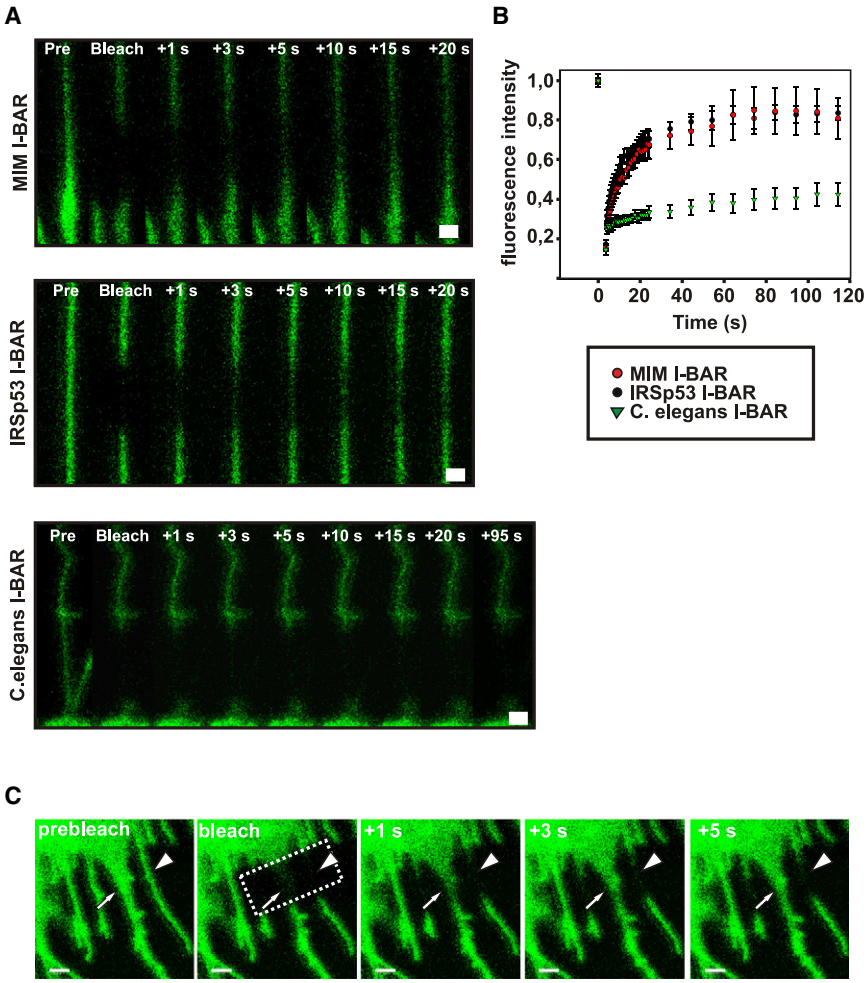

Figure 6. Dynamics of I-BARs in Filopodia

(A) Representative images from FRAP analysis of the association MIM and IRSp53 and *C. elegans* I-BARs in filopodia. Scale bars represent 1 μm.

(B) Analysis of FRAP recovery. Both IRSp53 and MIM I-BARs display rapid recovery after photobleaching, whereas *C. elegans* I-BAR recovers very slowly. Data represent mean values ± SEM calculated from 6–12 FRAP series.

(C) FRAP analysis of a cell transfected with a construct expressing *C. elegans* I-BAR demonstrates that the narrow filopodia with regular diameter (arrowhead) recover very slowly, whereas a thicker *C. elegans* I-BAR containing filopodia with a more variable diameter (arrow) recovers within a few seconds. Scale bars represent 1.5 μm.

the mechanisms by which I-BAR domains deform phospholipid-rich membranes. Time-lapse imaging of GUVs and cryo-EM analysis provided direct evidence that I-BAR domains bind to the inner surface of membrane tubules and thus explain why I-BARs deform membranes in the opposite direction to that of BAR and F-BAR domains. These data are supported by previous studies demonstrating that the lipid-binding interface of I-BAR domains displays an opposite geometry to that of BAR and F-BAR domains, and that based on electron tomography, the I-BAR domain-induced membrane tubules appear to invaginate toward the interior of vesicles [28–31]. Interestingly, our data also revealed surprising variation in the mechanisms by which evolutionarily distinct classes of I-BAR domains generate membrane curvature (Figure 7).

A general feature among BAR/F-BAR domains is that they bind phospholipids through positively charged residues that are located at their concave surface [1]. We show that upon membrane binding, I-BAR domains induce strong $PI(4,5)P_2$ clustering. Also, the N-BAR domain of amphiphysin clustered $PI(4,5)P_2$, although somewhat less efficiently, suggesting that $PI(4,5)P_2$ clustering may be a general feature among BAR domains. The stronger $PI(4,5)P_2$ clustering by I-BAR domains compared to amphiphysin N-BAR domain is in agreement with the stronger net-positive electrostatic potentials of I-BARs. It is also important to note that increased packing of phosphoinositides induces local lateral asymmetry in the inner leaflet of the plasma membrane, thereby altering the physical properties of the membrane. This might also have an influence in cell signaling [40]. How proteins regulate the distribution of various lipids in the membranes is an important but poorly understood subject. The data presented here suggest that I-BAR domains and BAR/F-BAR domains are capable of inducing the formation of $PI(4,5)P_2$-rich microdomains at the plasma membrane.

A subset of BAR domains, N-BARs, employs an additional N-terminal helix to enhance membrane curvature sensing and/or generation [17]. Our data show that a similar mechanism is used in the membrane interactions of a subset of I-BAR domains. However, in contrast to the amphipathic α helix of N-BARs, which runs parallel with the membrane at the level of the lipid headgroups, the N-terminal α helix of MIM I-BAR inserts deeper into the membrane bilayer. In the case of N-BAR domains, some controversy exists concerning whether or not the N-terminal α helix plays a critical role in membrane curvature sensing and/or membrane deformation [17, 18, 41]. Our data show that at least in I-BAR domains, insertion of the N-terminal α helix into the membrane bilayer is not critical to membrane deformation. However, this helix appears to enhance the membrane tubulation efficiency of MIM I-BAR in vivo and may thus enable this domain to bind flat membranes or membranes with positive curvature more efficiently. Additionally, insertion of the helix into the membrane bilayer increases the diameter of I-BAR-induced membrane tubules. This can be explained by the fact that although the shape and electrostatic potential of I-BARs work toward inducing negative membrane curvature, the insertion of an amphipathic/hydrophobic helix into the inner leaflet of the membrane tubule may bend the membrane in the opposite direction if the helix is oriented in the membrane perpendicularly to the I-BAR domain.

In addition to differences in membrane insertion of the N-terminal α helix, I-BAR domains also display significant differences in the dynamics of filopodia association. Whereas mammalian I-BARs display dynamic association with filopodia, the *C. elegans* I-BAR is much more stably associated with filopodia. This suggests that like F-BAR domains [26], the *C. elegans* I-BAR domain may form a helical scaffold inside

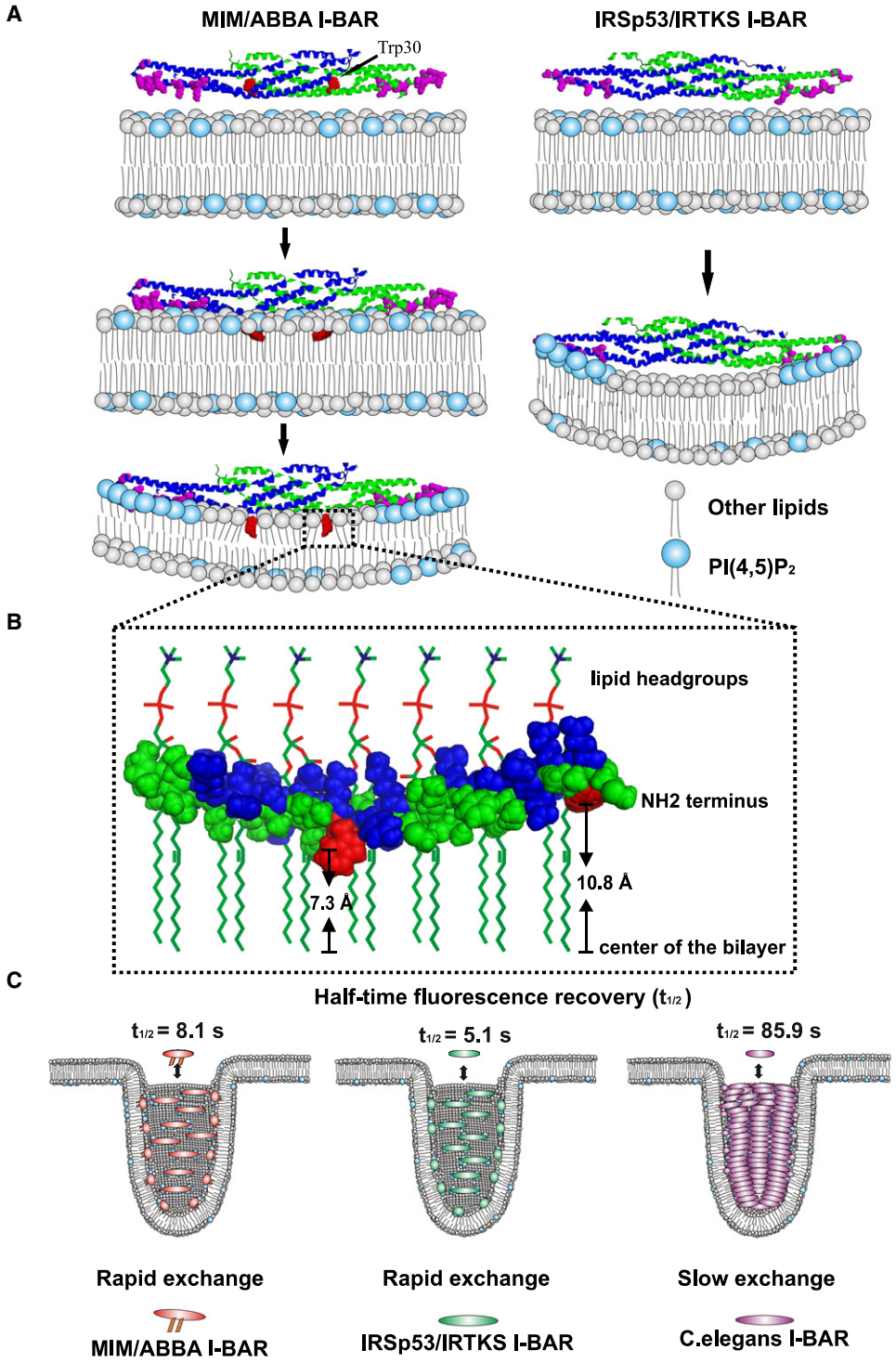

Figure 7. A Working Model for the Mechanisms of I-BAR Domain-Induced Deformation

(A) The MIM/ABBA subfamily of I-BAR domains insert their N-terminal amphiphatic helix into the bilayer independently of their positively charged phospholipid-binding interface. Subsequently, strong electrostatic interactions between the positively charged poles of MIM/ABBA I-BARs and the negatively charged $PI(4,5)P_2$ headgroups induce clustering of $PI(4,5)P_2$ and generation of membrane curvature because of the convex geometry of the lipid-binding interface of the domain. In contrast, IRSp53 and IRTKS I-BAR domains rely solely on their electrostatic interactions in membrane binding and tubulation. The structures of mouse MIM I-BAR (ID: 2D1L) and human IRSp53 I-BAR (ID: 1Y2O) domains are from the Protein Data Bank.

(B) A schematic model for the insertion of the N-terminal helix of MIM into the membrane. Tryptophans are in red, other hydrophobic residues in green, and polar residues in blue. Trp4 and Trp30 are located approximately 10.8 Å and 7.3 Å from the center of the bilayer, respectively.

(C) Based on FRAP experiments, the MIM and IRSp53 I-BARs display dynamic association with filopodia ($t_{1/2}$ = 8.1 s and 5.1 s, respectively), suggesting that these domains make significantly weaker intermolecular contacts between adjacent domains as compared to *C. elegans* I-BAR domain ($t_{1/2}$ = 85.9 s). Thus, *C. elegans* I-BAR domain may form a more stabile lattice inside the membrane tubule as compared to vertebrate I-BAR domains.

the membrane tubules through lateral and/or tip-to-tip interactions. This would also provide an explanation for our observation that IRSp53 I-BAR, which induce the formation of membrane tubules with a similar diameter than the *C. elegans* I-BAR, does not colocalize with the *C. elegans* I-BAR when coexpressed in cells. Although the association of MIM and IRSp53 I-BARs with filopodia is dynamic and the filopodia induced by these domains are somewhat irregular in diameter, these domains also appear to localize to membrane tubules cooperatively. This may result either from relatively weak intermolecular interactions between these I-BARs in membrane tubules or from negative membrane curvature sensing that would make it energetically more favorable for these domains to bind membranes that already display appropriate negative curvature.

It is an open question whether I-BAR domains, in full-length endogenous proteins, sense membrane curvature, and thus direct the protein with its possible interaction partners to the sites of negative membrane curvature, or whether these domains actively generate membrane curvature in cells. From our data we propose that MIM and ABBA I-BAR domains insert an amphipathic N-terminal α helix into the membrane and can thus perhaps sense positive membrane curvature before generating negative membrane curvature through their electrostatic interactions. This suggests that at least the role of these two I-BAR domains in the context of full-length proteins is to actively generate membrane curvature. This hypothesis is in agreement with recent studies demonstrating that IRSp53 and ABBA are involved in membrane ruffling and the formation of filopodia in cells [36, 42–44], with theoretical studies concerning the role of membrane deformation in membrane protrusions [45] and with the localization of filopodia markers to the I-BAR domain-induced membrane protrusions (Figure S5). In the future, it will be important to reveal how these domains in the context of full-length proteins and their interaction partners contribute to the formation of morphologically distinct membrane protrusions in cells.

Experimental Procedures

Electron Microscopy

For cryo-EM, 0.1–0.5 mg/ml vesicles (described in Supplemental Data) were mixed with 0.05–0.25 mg/ml protein in a 2:1 ratio (mass:mass) in 20 mM HEPES (pH 7.5), 100 mM NaCl. After addition of the protein to the lipids, the samples were slowly cooled in a PCR machine as previously described [26]. Samples were prepared on copper holey carbon film grids (Quantifoil), blotted from the back, and vitrified in liquid ethane [46]. A Gatan 626 cryostage was used to observe the sample in a FEI Tecnai F20 field emission gun transmission electron microscope at 200 kV under low-dose conditions at −180°C. Electron micrographs were recorded on Kodak SO-163 film at a magnification of 50,000× and defocus values ranging from −1.6 to −3.8 μm. The film was developed in full-strength D19 for 12 min. Micrographs were digitized at 7 μm step size on a Zeiss Photoscan TD scanner giving a pixel size of 1.4 Å/pixel. The program Digital Micrograph (Gatan Inc.) was used for calculating density profiles from the digitized images. Fixed samples for transmission electron microscopy were prepared by mixing 6 μM protein (in the case of IRTKS 20 μM) with 166 μM multilamellar vesicles in 20 mM HEPES (pH 7.5), 100 mM NaCl. Sample preparation and microscopy were done as described [30] with the exception that all images were taken from 120 nm thick sections.

Cell Culture, Transfections, and Immunofluorescence

U2OS human osteosarcoma cells were cultured in D-MEM containing 10% FCS and antibiotics. Transient transfections were done with Fugene6 reagent (Roche) according to the manufacturer's instructions and, depending on the application, cells were imaged or fixed with 4% PFA the next day, 20–30 hr after transfection. For visualization of Myosin-10, cells were incubated with 2 μg/ μl myosin-10 antibody [39] (R. Cheney, University of North Carolina) with Alexa-568 conjugated secondary antibody (dilution 1:200).

Light Microscopy and Image Analysis

Fixed cells were imaged with a fluorescence microscope (AX70 Provis; Olympus) equipped with a charge-coupled device camera (DP70; Olympus) with PlanApo 60x/1.40 (oil) or UPlanApo 100x/1.35 (oil) objectives (Olympus). Images were acquired with AnalySIS software (Olympus). Live-cell and GUV imaging were done with an inverted microscope (IX-71; Olympus) equipped with a Polychrome IV monochromator (TILL Photonics) and Andor iXon (Andor) camera. For cell imaging, a heated sample environment (+37°C) with constant CO_2 flow was used, whereas GUVs were imaged at RT without CO_2. All imaging was done with a UPlanSApo 60xW/1.20 (water) objective. Image acquirement was done with TILL Vision 4 (TILL Photonics) software. Video processing, measurement of intensity profiles, and amount of filopodia and the width of membrane tubes were done with Image-pro plus 5.1 software. Movies S1 and S2 and the still images shown in Figure 2B were deconvolved with AutoQuantX AutoDeblur (Media Cybernetics, Inc.). The width of membrane tubes was measured from EM images taken with 23,000× magnification from 2–3 grids. For filopodia quantification, all peripheral protrusions that were longer than 0.6 μm and narrower than 0.6 μm were calculated from more than 30 cells derived from three independent experiments. Image processing was carried out with Adobe Photoshop 7.0.

FRAP Experiments

FRAP experiments were carried out with Leica TCS SP2 AOBS confocal microscope, APO 63x/1.2 W Corr/0.17 CS (water) objective and Argon 488 nm laser line (70 mW) at +37°C with constant CO_2 supply. GFP-tagged I-BAR constructs were bleached with a rectangular region of 18 μm^2 from the midregion of protruding filopodia with Flymode FRAP application (Leica Lite 2.61.1537 confocal software). Bleaching was done with 100% and imaging the recovery with 4% laser power. The recovery was monitored every 0.5–10 s over a total period of 160 s. The intensity of the bleached region was normalized to a nonbleached region to reduce the error caused by normal photobleaching during the imaging process. From each sample, 6–12 filopodia were analyzed and the average was plotted on a scatter plot (SigmaPlot) and the recovery half-time ($t_{1/2}$) was analyzed from the plot. The prebleach value was normalized to 1. Images for FRAP panel were acquired with Imaris (Bitplane, Inc.) and Adobe Photoshop software.

Statistical Analysis

All graphs and statistical analyses were done with SigmaPlot 9.0 or SPSS 15.0 with appropriate applications. Error bars in graphs indicate ±SEM. Differences between independent groups were tested with Student's t test (two groups) or with one-way ANOVA (three or more groups) with Tukey as a post hoc test. Significance level was set at 0.05.

Supplemental Data

Supplemental Data include Supplemental Experimental Procedures, five figures, and two movies and can be found with this article online at http://www.current-biology.com/supplemental/S0960-9822(08)01684-9.

Acknowledgments

We thank Anna-Liisa Nyfors and the staff at the electron and light microscopy units (Institute of Biotechnology, University of Helsinki) for technical assistance. Richard Cheney, Frank Gertler, Johanna Ivaska, Yuri Kohara, and Danijela Vignjevic are acknowledged for providing antibodies and GFP-fusion constructs, and Petri Auvinen is thanked for critical reading of the manuscript. This study was supported by grants from Academy of Finland, Finnish Cancer Foundation (to P. Lappalainen and H.Z.) and Biocentrum Helsinki (to P. Lappalainen and S.J.B.). J.S. was supported by a fellowship from Helsinki Graduate School in Biotechnology and Molecular Biology.

Received: September 5, 2008
Revised: November 26, 2008
Accepted: December 8, 2008
Published online: January 15, 2009

References

1. Zimmerberg, J., and Kozlov, M.M. (2006). How proteins produce cellular membrane curvature. Nat. Rev. Mol. Cell Biol. *1*, 9–19.
2. McMahon, H.T., and Gallop, J.L. (2005). Membrane curvature and mechanisms of dynamic cell membrane remodelling. Nature *7068*, 590–596.
3. Daumke, O., Lundmark, R., Vallis, Y., Martens, S., Butler, P.J., and McMahon, H.T. (2007). Architectural and mechanistic insights into an EHD ATPase involved in membrane remodelling. Nature *7164*, 923–927.
4. Martens, S., and McMahon, H.T. (2008). Mechanisms of membrane fusion: disparate players and common principles. Nat. Rev. Mol. Cell Biol. *7*, 543–556.
5. Roux, A., Uyhazi, K., Frost, A., and De Camilli, P. (2006). GTP-dependent twisting of dynamin implicates constriction and tension in membrane fission. Nature *7092*, 528–531.
6. Hu, N.J., Bradshaw, J., Lauter, H., Buckingham, J., Solito, E., and Hofmann, A. (2008). Membrane-induced folding and structure of membrane-bound annexin A1 N-terminal peptides: implications for annexin-induced membrane aggregation. Biophys. J. *5*, 1773–1781.
7. Hanson, P.I., Roth, R., Lin, Y., and Heuser, J.E. (2008). Plasma membrane deformation by circular arrays of ESCRT-III protein filaments. J. Cell Biol. *2*, 389–402.
8. Lata, S., Schoehn, G., Jain, A., Pires, R., Piehler, J., Gottlinger, H.G., and Weissenhorn, W. (2008). Helical structures of ESCRT-III are disassembled by VPS4. Science *321*, 1354–1357.
9. Wise, C.A., Gillum, J.D., Seidman, C.E., Lindor, N.M., Veile, R., Bashiardes, S., and Lovett, M. (2002). Mutations in CD2BP1 disrupt binding to PTP PEST and are responsible for PAPA syndrome, an autoinflammatory disorder. Hum. Mol. Genet. *8*, 961–969.
10. Endris, V., Wogatzky, B., Leimer, U., Bartsch, D., Zatyka, M., Latif, F., Maher, E.R., Tariverdian, G., Kirsch, S., Karch, D., et al. (2002). The novel Rho-GTPase activating gene MEGAP/ srGAP3 has a putative role in severe mental retardation. Proc. Natl. Acad. Sci. USA *18*, 11754–11759.
11. Nicot, A.S., Toussaint, A., Tosch, V., Kretz, C., Wallgren-Pettersson, C., Iwarsson, E., Kingston, H., Garnier, J.M., Biancalana, V., Oldfors, A., et al. (2007). Mutations in amphiphysin 2 (BIN1) disrupt interaction with dynamin 2 and cause autosomal recessive centronuclear myopathy. Nat. Genet. *9*, 1134–1139.
12. Di Paolo, G., Sankaranarayanan, S., Wenk, M.R., Daniell, L., Perucco, E., Caldarone, B.J., Flavell, R., Picciotto, M.R., Ryan, T.A., Cremona, O., et al. (2002). Decreased synaptic vesicle recycling efficiency and cognitive deficits in amphiphysin 1 knockout mice. Neuron *5*, 789–804.
13. Itoh, T., Erdmann, K.S., Roux, A., Habermann, B., Werner, H., and De Camilli, P. (2005). Dynamin and the actin cytoskeleton cooperatively regulate plasma membrane invagination by BAR and F-BAR proteins. Dev. Cell *6*, 791–804.
14. Steinberg, J.P., Takamiya, K., Shen, Y., Xia, J., Rubio, M.E., Yu, S., Jin, W., Thomas, G.M., Linden, D.J., and Huganir, R.L. (2006). Targeted in vivo mutations of the AMPA receptor subunit GluR2 and its interacting protein PICK1 eliminate cerebellar long-term depression. Neuron *6*, 845–860.
15. Frost, A., De Camilli, P., and Unger, V.M. (2007). F-BAR proteins join the BAR family fold. Structure *7*, 751–753.
16. Peter, B.J., Kent, H.M., Mills, I.G., Vallis, Y., Butler, P.J., Evans, P.R., and McMahon, H.T. (2004). BAR domains as sensors of membrane curvature: the amphiphysin BAR structure. Science *5657*, 495–499.
17. Gallop, J.L., Jao, C.C., Kent, H.M., Butler, P.J., Evans, P.R., Langen, R., and McMahon, H.T. (2006). Mechanism of endophilin N-BAR domain-mediated membrane curvature. EMBO J. *12*, 2898–2910.
18. Masuda, M., Takeda, S., Sone, M., Ohki, T., Mori, H., Kamioka, Y., and Mochizuki, N. (2006). Endophilin BAR domain drives membrane curvature by two newly identified structure-based mechanisms. EMBO J. *12*, 2889–2897.
19. Pylypenko, O., Lundmark, R., Rasmuson, E., Carlsson, S.R., and Rak, A. (2007). The PX-BAR membrane-remodeling unit of sorting nexin 9. EMBO J. *22*, 4788–4800.
20. Li, J., Mao, X., Dong, L.Q., Liu, F., and Tong, L. (2007). Crystal structures of the BAR-PH and PTB domains of human APPL1. Structure *5*, 525–533.
21. Zhu, G., Chen, J., Liu, J., Brunzelle, J.S., Huang, B., Wakeham, N., Terzyan, S., Li, X., Rao, Z., Li, G., et al. (2007). Structure of the APPL1 BAR-PH domain and characterization of its interaction with Rab5. EMBO J. *14*, 3484–3493.
22. Tsujita, K., Suetsugu, S., Sasaki, N., Furutani, M., Oikawa, T., and Takenawa, T. (2006). Coordination between the actin cytoskeleton and membrane deformation by a novel membrane tubulation domain of PCH proteins is involved in endocytosis. J. Cell Biol. *2*, 269–279.
23. Shimada, A., Niwa, H., Tsujita, K., Suetsugu, S., Nitta, K., Hanawa-Suetsugu, K., Akasaka, R., Nishino, Y., Toyama, M., Chen, L., et al. (2007). Curved EFC/F-BAR-domain dimers are joined end to end into a filament for membrane invagination in endocytosis. Cell *4*, 761–772.
24. Henne, W.M., Kent, H.M., Ford, M.G., Hegde, B.G., Daumke, O., Butler, P.J., Mittal, R., Langen, R., Evans, P.R., and McMahon, H.T. (2007). Structure and analysis of FCHo2 F-BAR domain: a dimerizing and membrane recruitment module that effects membrane curvature. Structure *7*, 839–852.
25. Heath, R.J., and Insall, R.H. (2008). F-BAR domains: multifunctional regulators of membrane curvature. J. Cell Sci. *121*, 1951–1954.
26. Frost, A., Perera, R., Roux, A., Spasov, K., Destaing, O., Egelman, E.H., De Camilli, P., and Unger, V.M. (2008). Structural basis of membrane invagination by F-BAR domains. Cell *5*, 807–817.
27. Yamagishi, A., Masuda, M., Ohki, T., Onishi, H., and Mochizuki, N. (2004). A novel actin bundling/filopodium-forming domain conserved in insulin receptor tyrosine kinase substrate p53 and missing in metastasis protein. J. Biol. Chem. *15*, 14929–14936.
28. Millard, T.H., Bompard, G., Heung, M.Y., Dafforn, T.R., Scott, D.J., Machesky, L.M., and Futterer, K. (2005). Structural basis of filopodia formation induced by the IRSp53/MIM homology domain of human IRSp53. EMBO J. *2*, 240–250.
29. Lee, S.H., Kerff, F., Chereau, D., Ferron, F., Klug, A., and Dominguez, R. (2007). Structural basis for the actin-binding function of missing-in-metastasis. Structure *2*, 145–155.
30. Mattila, P.K., Pykalainen, A., Saarikangas, J., Paavilainen, V.O., Vihinen, H., Jokitalo, E., and Lappalainen, P. (2007). Missing-in-metastasis and IRSp53 deform PI(4,5)P2-rich membranes by an inverse BAR domain-like mechanism. J. Cell Biol. *7*, 953–964.
31. Suetsugu, S., Murayama, K., Sakamoto, A., Hanawa-Suetsugu, K., Seto, A., Oikawa, T., Mishima, C., Shirouzu, M., Takenawa, T., and Yokoyama, S. (2006). The RAC binding domain/IRSp53-MIM homology domain of IRSp53 induces RAC-dependent membrane deformation. J. Biol. Chem. *46*, 35347–35358.
32. Mattila, P.K., Salminen, M., Yamashiro, T., and Lappalainen, P. (2003). Mouse MIM, a tissue-specific regulator of cytoskeletal dynamics, interacts with ATP-actin monomers through its C-terminal WH2 domain. J. Biol. Chem. *10*, 8452–8459.
33. Woodings, J.A., Sharp, S.J., and Machesky, L.M. (2003). MIM-B, a putative metastasis suppressor protein, binds to actin and to protein tyrosine phosphatase delta. Biochem. J. *371*, 463–471.
34. Scita, G., Confalonieri, S., Lappalainen, P., and Suetsugu, S. (2008). IRSp53: crossing the road of membrane and actin dynamics in the formation of membrane protrusions. Trends Cell Biol. *2*, 52–60.
35. Sens, P., Johannes, L., and Bassereau, P. (2008). Biophysical approaches to protein-induced membrane deformations in trafficking. Curr. Opin. Cell Biol. *4*, 476–482.
36. Saarikangas, J., Hakanen, J., Mattila, P.K., Grumet, M., Salminen, M., and Lappalainen, P. (2008). ABBA regulates plasma-membrane and actin dynamics to promote radial glia extension. J. Cell Sci. *121*, 1444–1454.
37. Zaritsky, A., Parola, A.H., Abdah, M., and Masalha, H. (1985). Homeoviscous adaptation, growth rate, and morphogenesis in bacteria. Biophys. J. *2*, 337–339.
38. Mattila, P.K., and Lappalainen, P. (2008). Filopodia: molecular architecture and cellular functions. Nat. Rev. Mol. Cell Biol. *6*, 446–454.
39. Berg, J.S., Derfler, B.H., Pennisi, C.M., Corey, D.P., and Cheney, R.E. (2000). Myosin-X, a novel myosin with pleckstrin homology domains, associates with regions of dynamic actin. J. Cell Sci. *113*, 3439–3451.
40. Janmey, P.A., and Kinnunen, P.K. (2006). Biophysical properties of lipids and dynamic membranes. Trends Cell Biol. *10*, 538–546.
41. Farsad, K., Ringstad, N., Takei, K., Floyd, S.R., Rose, K., and De Camilli, P. (2001). Generation of high curvature membranes mediated by direct endophilin bilayer interactions. J. Cell Biol. *2*, 193–200.
42. Suetsugu, S., Kurisu, S., Oikawa, T., Yamazaki, D., Oda, A., and Takenawa, T. (2006). Optimization of WAVE2 complex-induced actin polymerization by membrane-bound IRSp53, PIP(3), and Rac. J. Cell Biol. *4*, 571–585.

43. Disanza, A., Mantoani, S., Hertzog, M., Gerboth, S., Frittoli, E., Steffen, A., Berhoerster, K., Kreienkamp, H.J., Milanesi, F., Di Fiore, P.P., et al. (2006). Regulation of cell shape by Cdc42 is mediated by the synergic actin-bundling activity of the Eps8-IRSp53 complex. Nat. Cell Biol. *12*, 1337–1347.
44. Lim, K.B., Bu, W., Goh, W.I., Koh, E., Ong, S.H., Pawson, T., Sudhaharan, T., and Ahmed, S. (2008). The Cdc42 effector IRSp53 generates filopodia by coupling membrane protrusion with actin dynamics. J. Biol. Chem. *29*, 20454–20472.
45. Veksler, A., and Gov, N.S. (2007). Phase transitions of the coupled membrane-cytoskeleton modify cellular shape. Biophys. J. *93*, 3798–3810.
46. Adrian, M., Dubochet, J., Lepault, J., and McDowall, A.W. (1984). Cryo-electron microscopy of viruses. Nature *5954*, 32–36.